Impact of Temperature on Seebeck Coefficient of Nodal Line Semimetal in Molecular Conductor

Yoshikazu Suzumura *

Posted Date: 10 June 2024

doi: 10.20944/preprints202406.0543.v1

Keywords: Seebeck coefficient; nodal line semimetal; single-component molecular conductor; spectral conductivity; DOS; tight-binding model

 doi:10.20944/preprints202406.0543.v1

Article

Impact of Temperature on Seebeck Coefficient of Nodal Line Semimetal in Molecular Conductor

Yoshikazu Suzumura

Department of Physics, Nagoya University, Nagoya 464-8602, Japan; suzumura@s.phys.nagoya-u.ac.jp

Abstract: We examine the impact of temperature (T) on the Seebeck coefficient S, i.e., the T dependence of S for the single-component molecular conductor [Pd(dddt)$_2$] (dddt = 5,6-dihydro-1,4-dithiin-2,3-dithiolate) with a half-filled band, where the coefficient is obtained from a ratio of the thermal conductivity to the electrical conductivity. The conductor exhibits Dirac electrons with a nodal line, which shows the energy variation around the chemical potential and the density of states (DOS) with a minimum. Using a three-dimensional tight-binding (TB) model in the presence of both impurity and electron–phonon (e–p) scatterings, we study the Seebeck coefficient S_y for the molecular stacking and the most conducting direction. The impact of T on S_y exhibits a sign change, where $S_y > 0$ with a maximum at high temperatures and $S_y < 0$ with a minimum at low temperatures. The T dependence of S_y suggests that the contribution from the conduction (valence) band is dominant at low (high) temperatures. The result is examined using a spectral conductivity $\sigma_y(\epsilon, T)$ as a function of the energy ϵ close to the chemical potential μ. Further, the Seebeck coefficients for perpendicular directions (x and z) are examined, to show both S_x and S_z being positive and no sign change in contrast to S_y.

Keywords: Seebeck coefficient; nodal line semimetal; single-component molecular conductor; spectral conductivity; DOS; tight-binding model

1. Introduction

Massless Dirac fermions exhibit characteristic properties of electrons, which originate from the energy band with a linear dispersion [1]. The Dirac electron in a bulk system has been found in the following two kinds of molecular conductors [2,3].

One is the organic conductor α-(BEDT-TTF)$_2$I$_3$ under pressures [(BEDT-TTF = bis(ethylenedithio) tetrathiafulvalene], in which the Dirac cone is discovered [4,5] using the tight-binding (TB) model with the transfer energy estimated by the extended Hückel method [6–8]. The conductor exhibits a zero-gap state (ZGS) with the density of states (DOS), which vanishes linearly at the Fermi energy. The Dirac cone was confirmed by the first-principles DFT calculation. [9]. Further, a two band model [10,11] has been proposed to examine the Dirac electron in the organic conductor. Several properties of the Dirac cone appear in the temperature (T) dependence of physical quantities. The reversal of the sign of the Hall coefficient, which occurs for the chemical potential being equal to the energy of the Dirac point, was proposed theoretically [12] and was also observed experimentally in the Hall conductivity [13]. The conductivity of Dirac electrons has been examined using a two-band model with the conduction and valence bands. The static conductivity at absolute zero temperature remains finite with a universal value, i.e., independent of the magnitude of the impurity scattering owing to a quantum effect [14]. At finite temperatures, the conductivity depends on the magnitude of the impurity scattering, Γ_0, which is proportional to the inverse of the life-time by the disorder. With increasing temperature, the conductivity increases for $\Gamma_0 \ll T$ [15]. Although a monotonic increase in the conductivity is expected, the measured conductivity (or resistivity) on the above organic conductor shows an almost constant behavior at high temperatures [16–20]. Noting the electron-phonon (e-p) interaction enhances the resistivity of the conventional metal at high temperatures, a nearly constant conductivity at high temperatures is explained by adding an acoustic phonon scattering to a two-band model with the Dirac cone [21].

Another Dirac electron system has been found in a single-component molecular conductor, [Pd(dddt)$_2$], (dddt = 5,6-dihydro-1,4-dithiin-2,3-dithiolate) [3] which exhibits a three-dimensional

 doi:10.20944/preprints202406.0543.v1

Dirac electron system under a high pressure with almost temperature independent resistivity [22]. First-principles calculations [23] show a three-dimensional Dirac electron system, consisting of HOMO (Highest Occupied Molecular Orbital) and LUMO (Lowest Unoccupied Molecular Orbital) bands, and a TB model exhibits a loop of Dirac points [24]. This system is one of systems, called as a nodal line semimetal, i.e., a loop of Dirac points [25–27]. There are several studies on the effective Hamiltonian, where a general two-band model is introduced [28] and the explicit calculation is performed for the nodal line semimetal [29]. The conductivity was also examined [30] to comprehend the almost temperature independent conductivity. Recently a TB model was improved using the crystal structure, which was obtained under high pressure [31]. This band calculation shows the DOS, which depends linearly in a wide region of the energy being compatible with the temperature corresponding to almost constant conductivity. Thus, we recalculated the almost constant resistivity in $[Pd(dddt)_2]$ using the newly found TB model and by taking account of both impurity and acoustic phonon scatterings [32]. It was shown that an interplay of two kinds of scattering explains the T dependence of the resistivity obtained by the experiment. In addition to two-dimensional systems with Dirac points, three-dimensional system with nodal line semimetal is of interest due to anisotropic conductivity and a common feature of the almost constant conductivity.

Seebeck coefficient, which is proportional to a ratio of the thermal conductivity to the electrical conductivity, is a quantity displaying a competition between the conduction and valence bands in Dirac electrons. It does not depend on details of the e–p interaction and impurity scattering. The general formula has been established in terms of linear response theory [33–35]. For the Seebeck coefficient, S_ν ($\nu =$ x and y) of the organic conductor α-(BEDT-TTF)$_2$I$_3$, there are experiments on the T dependence under hydrostatic pressures , [36,37] where the sign of S_x (perpendicular to the molecular stacking axis) is positive except for low temperatures depending on samples. There are theoretical studies for S_y at ambient pressure with a correlation [38] and for S_x under a uniaxial pressure [39] Using a TB model, [40] which has been derived from the DFT calculation with the experimental lattice structure, it has been shown that the Seebeck coefficient under hydrostatic pressures is positive, i.e., $S_x, S_y > 0$ at finite temperatures. However, the Seebeck coefficient of the nodal line semimetal has not yet been clarified.

In the present paper, we examine the Seebeck effect of $[Pd(dddt)_2]$ in addition to the conductivity, [32] where the T dependence of μ takes a crucial role. In Section 2, the model and formulation for the Seebeck coefficient of $[Pd(dddt)_2]$ with 1/2-filled band are given. The electronic states are examined by calculating the energy band, the nodal line of Dirac points, DOS, and the T dependence of the chemical potential. In Section 3, we present the Seebeck coefficient and the electric conductivity for both directions being parallel and perpendicular to the molecular stacking (y) axis. They are analyzed in terms of the spectral conductivity [39] Section 4 is devoted to summary and discussion.

2. Formulation

2.1. Model

We consider a two-dimensional Dirac electron system given by

$$H = H_{\rm TB} + H_{\rm p} + H_{\rm e-p} + H_{\rm imp} \, . \tag{1}$$

Here, $H_{\rm TB}$ denotes a TB model of the single-component molecular conductor consisting of four molecules per unit cell, which is shown below. The second term denotes the harmonic phonon given by $H_{\rm p} = \sum_{\boldsymbol{q}} \omega_{\boldsymbol{q}} b^\dagger_{\boldsymbol{q}} b_{\boldsymbol{q}}$ with $\omega_{\boldsymbol{q}} = v_s|\boldsymbol{q}|$ and $\hbar$ =1. The third term is the electron–phonon (e–p) interaction with a coupling constant $g_{\boldsymbol{q}}$, [41]

$$H_{\rm e-p} = \sum_{k,\gamma} \sum_{\boldsymbol{q}} g_{\boldsymbol{q}} c_\gamma(\boldsymbol{k}+\boldsymbol{q})^\dagger c_\gamma(\boldsymbol{k})(b_{\boldsymbol{q}} + b^\dagger_{-\boldsymbol{q}}) \, , \tag{2}$$

 doi:10.20944/preprints202406.0543.v1

with $c_\gamma(\boldsymbol{k}) = \sum_\alpha d_{\alpha\gamma} a_\alpha(\boldsymbol{k})$, which is obtained by the diagonalization of $H_{\rm TB}$ as shown later. The e–p scattering is considered within the same band (i.e., intraband) owing to the energy conservation with $v \gg v_s$, where $v \simeq 0.05$ [10] denotes the averaged velocity of the Dirac cone. The last term of Equation (1), $H_{\rm imp}$, denotes a normal impurity scattering.

Figure 1 displays the crystal structure of [Pd(dddt)$_2$] [3,24] which consists of four molecules (1, 2, 3, and 4) with HOMO and LUMO per unit cell providing eight molecular orbitals. These molecules are located on two kinds of layers with the x–y plane, where the layer 1 includes molecules 1 and 3, and the layer 2 includes molecules 2 and 4, respectively. The z axis is perpendicular to the x–y plane of the layers 1 and 2 forming a three-dimensional system.

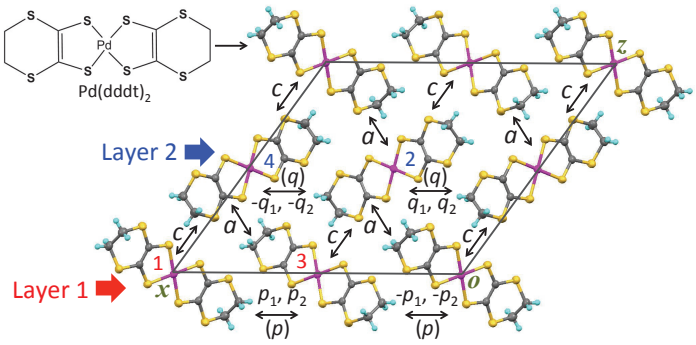

Figure 1. (Color online) Crystal structure of [Pd(dddt)$_2$] shown in the x–z plane, [24] where the molecule is stacked along the y direction perpendicular to the plane. Layer 1 (molecules 1 and 3) and Layer 2 (molecules 2 and 4) are parallel to the x–y plane and alternated along the z direction. The notations x, y, and z correspond to a, b , and c of the conventional crystallography.

A revised TB model corresponding to Figure 1 has been recently obtained using the crystal structure observed under pressure [31]. There are several kinds of transfer energies between two molecular orbitals, which are listed in Table 1. The interlayer energies in the z direction are given by a (1 and 2 molecules, and 3 and 4 molecules), and c (1 and 4 molecules, and 2 and 3 molecules). The intralayer energies in the x–y plane are given by p (1 and 3 molecules) and q (2 and 4 molecules) and b (along the molecular stacking y axis). Further, these energies are classified by three kinds of transfer energies given by HOMO-HOMO (H), LUMO-LUMO (L), and HOMO-LUMO (HL).

Table 1. Transfer energies for P=5.9GPa, [31] which are multiplied by 10^{-3}eV. The energy difference between the HOMO and LUMO is taken as ΔE = 0.696eV.

	H − H	L − L	H − L	
$b1$	209.3	−1.9	−51.2	(stacking)
$p1(p)$	28.1	−12.4	19.9	Layer 1
$p2$	—	—	17.1	
$b2$	49.9	−80.4	−67.2	(stacking)
$q1(q)$	10.8	8.1	9.3	Layer 2
$q2$	—	—	9.2	
$a1$	−28.2	14.6	−20.1	
$a2$	2.2	1.3	−1.7	Interlayer
$c1$	15.4	12.7	14.1	
$c2$	−3.9	15.8	−11.8	

 doi:10.20944/preprints202406.0543.v1

The TB model Hamiltonian in Equation (1) is expressed as

$$H_{\rm TB} = \sum_{i,j=1}^{N} \sum_{\alpha,\beta} t_{i,j;\alpha,\beta} \left|i,\alpha\right\rangle \left\langle j,\beta\right| \ , \tag{3}$$

where $t_{i,j;\alpha,\beta}$ are transfer energies between nearest-neighbor sites and $< i,\alpha|$ is a state vector. The spin degree of freedom is discarded. α,β = H1, H2, $\cdots$, L3, and L4.

Using a Fourier transform $|\alpha(\boldsymbol{k})\rangle = N^{-1/2}\sum_j \exp[-i\boldsymbol{k}\boldsymbol{r}_j] \ \ |j,\alpha\rangle$ with a wave vector $\boldsymbol{k} = (k_x, k_y, k_z)$, Equation (3) is rewritten as

$$H_{\rm TB} = \sum_{\boldsymbol{k}} |\Phi(\boldsymbol{k})\rangle \, \hat{H}(\boldsymbol{k}) \, \langle\Phi(\boldsymbol{k})| \ , \tag{4}$$

where $\langle\Phi(\boldsymbol{k})| = (\langle \mathrm{H1}|, \langle \mathrm{H2}|, \langle \mathrm{H3}|, \langle \mathrm{H4}|, \langle \mathrm{L1}|, \langle \mathrm{L2}|, \langle \mathrm{L3}|, \langle \mathrm{L4}|)$. We take the lattice constant as unity and then $0 < |k_x|, |k_y|, |k_z| < \pi$ in the first Brillouin zone. $\hat{H}(\boldsymbol{k})$ is 8×8 matrix Hamiltonian, where $h_{\alpha,\beta} = \left(\hat{H}(\boldsymbol{k})\right)_{\alpha,\beta}$. $h_{\alpha,\beta}(\boldsymbol{k})$ denotes a Fourier transform of $t_{i,j;\alpha,\beta}$ with a complex conjugate relation $h_{\alpha,\beta}(\boldsymbol{k}) = \overline{h_{\beta,\alpha}(\boldsymbol{k})}$. $\boldsymbol{k} = k_x a^* + k_y b^* + k_z c^* \equiv (k_x, k_y, k_z)$, where the k_y corresponds to the molecular staking axis and the lattice constant is taken as unity. Matrix elements $h_{\alpha,\beta}(\boldsymbol{k})$ are given in the previous work [32]. These energies in the unit of eV are listed in Table 1, where the gap between the energy of HOMO and that of LUMO is taken as $\Delta E = 0.696$eV to reproduce the energy band of the first principle calculation [24].

The energy band $E_j(\boldsymbol{k})$ and the wave function $|\Psi_j(\boldsymbol{k})\rangle$, $(j = 1, 2, \cdots, 8)$ are calculated from

$$\hat{H}(\boldsymbol{k}) \, |\Psi_j(\boldsymbol{k})\rangle = E_j(\boldsymbol{k}) \, |\Psi_j(\boldsymbol{k})\rangle \ , \tag{5}$$

where $E_1 > E_2 > \cdots > E_8$ and

$$|\Psi_j(\boldsymbol{k})\rangle = \sum_{\alpha} d_{\alpha j}(\boldsymbol{k}) \, |\alpha\rangle \ , \tag{6}$$

with α = H1, H2, H3, H4, L1, L2, L3, and L4.

2.2. Dirac Points and DOS

Since the electron close to the chemical potential is relevant for the electron-hole excitation, we consider only $E_4(\boldsymbol{k})$ and $E_5(\boldsymbol{k})$, i.e., the valence and conduction bands for the present calculation. Thus $E_4(\boldsymbol{k})$ and $E_5(\boldsymbol{k})$ are replaced by $E_+(\boldsymbol{k})$ and $E_-(\boldsymbol{k})$ for the calculation of the transport, while $E_\pm(\boldsymbol{k})$ represents not only the Dirac cone but also full dispersion of $E_4(\boldsymbol{k})$ and $E_5(\boldsymbol{k})$ in the first Brillouin zone. The present energy bands $E_\pm(\boldsymbol{k})$ provide a nodal line, i.e., a loop of the Dirac point $\boldsymbol{k}_{\rm D}$, which is obtained from

$$E_+(\boldsymbol{k}_{\rm D}) = E_-(\boldsymbol{k}_{\rm D}) \ . \tag{7}$$

The chemical potential $\mu = \mu(T)$ is determined self-consistently from

$$\begin{aligned} \frac{1}{N}\sum_{\boldsymbol{k}}\sum_{j=1}^{8} f(E_j(\boldsymbol{k}) - \mu(T)) \\ = \int_{-\infty}^{\infty} \mathrm{d}\omega \ D(\omega) f(\omega - \mu) = 4 \ , \end{aligned} \tag{8}$$

where $f(\omega) = 1/(\exp[\omega/T] + 1)$ with T being temperature in the unit of eV and $k_{\rm B} = 1$. Equation (8) is the condition of the half-filled band due to the HOMO and LUMO bands. $D(\omega)$ denotes a density of states (DOS) per spin and per unit cell, which is given by

$$D(\omega) \ = \ \frac{1}{N}\sum_{\boldsymbol{k}}\sum_{\gamma=\pm} \delta(\omega - E_\gamma(\boldsymbol{k})) \ , \tag{9}$$

where $\int \mathrm{d}\omega D(\omega) = 8$.

 doi:10.20944/preprints202406.0543.v1

2.3. Electric Transport

The conductivity is given by [42]

$$\sigma_\nu(T) = \int_{-\infty}^{\infty} d\epsilon \left(-\frac{\partial f(\epsilon-\mu)}{\partial \epsilon} \right) \times \sigma_\nu(\epsilon, T) \, . \tag{10}$$

The quantity $\sigma_\nu(\epsilon, T)$ denotes the spectral conductivity [39] for $\nu = x, y$ and z, which is calculated as (γ, γ' = 4 and 5)

$$\sigma_\nu(\epsilon, T) = \sum_{\gamma,\gamma'} \sigma_\nu^{\gamma\gamma'}(\epsilon, T) \, , \tag{11}$$

$$\begin{aligned} \sigma_\nu^{\gamma\gamma'}(\epsilon, T) &= \frac{e^2}{\pi\hbar N} \sum_{\boldsymbol{k}} v_{\gamma\gamma'}^{\nu}(\boldsymbol{k})^* v_{\gamma'\gamma}^{\nu}(\boldsymbol{k}) \\ &\times \frac{\Gamma_\gamma}{(\epsilon - E_\gamma(\boldsymbol{k}))^2 + \Gamma_\gamma^2} \times \frac{\Gamma_{\gamma'}}{(\epsilon - E_{\gamma'}(\boldsymbol{k}))^2 + \Gamma_{\gamma'}^2} \, , \end{aligned} \tag{12}$$

$$v_{\gamma\gamma'}^{\nu}(\boldsymbol{k}) = \sum_{\alpha\beta} d_{\alpha\gamma}(\boldsymbol{k})^* \frac{\partial h_{\alpha\beta}}{\partial k_\nu} d_{\beta\gamma'}(\boldsymbol{k}) \, . \tag{13}$$

$h = 2\pi\hbar$ and e denote Planck's constant and electric charge, respectively. The spectral conductivity depends on T due to the e–p interaction. In fact, Γ_γ denotes the damping of the electron of the γ band given by

$$\Gamma_\gamma = \Gamma + \Gamma_{\rm ph}^{\gamma} \, , \tag{14}$$

where the first term comes from the impurity scattering and the second term corresponding to the phonon scattering is given by [21,43]

$$\Gamma_{\rm ph}^{\gamma} = C_0 R \times T |\xi_{\gamma,\boldsymbol{k}}| \, , \tag{15a}$$

$$R = \frac{\lambda}{\lambda_0} \, , \tag{15b}$$

where $\lambda = |g_{\boldsymbol{q}}|^2/\omega_{\boldsymbol{q}}$, $\xi_{\gamma,\boldsymbol{k}} = E_\gamma(\boldsymbol{k}) - \mu$, $C_0 = 6.25\lambda_0/(2\pi v^2)$, $v = 0.05$ and $\lambda_0/2\pi v = 0.1$. λ_0 corresponds to λ for an organic conductor [44,45] and λ becomes independent of $|\boldsymbol{q}|$ for small $|\boldsymbol{q}|$. For parameters Γ and R, we take mainly Γ = 0.0003 and R=2 in the present numerial calculation.

In linear response theory, [33–35] the electric current density $\boldsymbol{j} = (j_x, j_y, j_z)$ is obtained by the electric field $\boldsymbol{E} = (E_x, E_y, E_z)$ and the temperature gradient ∇T, i.e., the ν (= x, y and z) component of the current density is expressed as

$$j_\nu = L_{11}^{\nu} E_\nu - L_{12}^{\nu} \nabla_\nu T/T \, , \tag{16}$$

where L_{11}^{ν} is the electrical conductivity σ_ν [42] as shown in Equation (10) and L_{12}^{ν} is the thermal conductivity. From (16), the Seebeck coefficient $S_\nu(T)$ is obtained by

$$S_\nu(T) = \frac{L_{12}^{\nu}}{T L_{11}^{\nu}} = \sum_{\gamma,\gamma'} S_\nu^{\gamma\gamma'}(T) \, , \tag{17}$$

where L_{11}^{ν} and L_{12}^{ν} are calculated as

$$L_{11}^{\nu} = \sigma_\nu(T) \, , \tag{18}$$

 doi:10.20944/preprints202406.0543.v1

$$L_{12}^{\nu} = \frac{-1}{e}\int_{-\infty}^{\infty} d\epsilon \left(-\frac{\partial f(\epsilon-\mu)}{\partial \epsilon}\right)(\epsilon-\mu)\sigma_{\nu}(\epsilon,T)\ , \tag{19}$$

and $S_{\nu}^{\gamma\gamma'}(T)$ is given by

$$S_{\nu}^{\gamma\gamma'} = \frac{-1}{e}\int_{-\infty}^{\infty} d\epsilon \left(-\frac{\partial f(\epsilon-\mu)}{\partial \epsilon}\right) \times(\epsilon-\mu)\sigma_{\nu}^{\gamma\gamma'}(\epsilon,T)\times\frac{1}{TL_{11}^{\nu}}\ . \tag{20}$$

Noting that $-\partial f(\epsilon-\mu)/\partial\epsilon$ is the even function of $\epsilon-\mu$, Equations (18) and (20) are calculated as

$$\sigma_{\nu}(\epsilon,T) = \sigma_{\nu}(\mu,T)+\sigma_{\nu}^{'}(\mu,T)(\epsilon-\mu) +\frac{1}{2}\sigma_{\nu}^{''}(\mu,T)(\epsilon-\mu)^2+\cdots, \tag{21}$$

$$eL_{12}^{\nu}(T) = -\frac{\pi^2}{3}\sigma_{\nu}^{'}(\mu,T)T^2-\frac{7\pi^4}{90}\sigma_{\nu}^{'''}(\mu,T)T^4 +\cdots. \tag{22}$$

At low temperatures, the sign change of $S_{\nu}(T)$ with decreasing T comes from the first term of Equation (22).

3. Electronic States

3.1. Energy Band

Figure 2a shows energy bands E_j (j=4 and 5) for the fixed $k_z = 0$, where E_4 (upper band) and E_5 (lower band) correspond to the conduction and valence bands, respectively. It is found that $E_4(\boldsymbol{k}_{\rm D}) = E_5(\boldsymbol{k}_{\rm D}) = \epsilon_{\rm D}$ and $E_4(\boldsymbol{k}) > \epsilon_{\rm D} > E_5(\boldsymbol{k})$. One-dimensional band is seen along k_y direction. Two bands correspond LUMO and HOMO, which are convex downward and upward respectively. When HOMO-LUMO coupling is absent, there is an intersection due to an overlapping. When HOMO-LUMO coupling is present, the intersection disappears due to a gap except for a Dirac point $\boldsymbol{k}_{\rm D}$. LUMO (HOMO) corresponds to E_4 (E_5), when LUMO band is larger than HOMO band. The relation is reversed when LUMO band is smaller than HOMO band. Figure 2b shows energy bands E_j (j=4 and 5) on the k_z–k_x plane for the fixed $k_y = 0$, The Dirac point exists between E_4 and E_5, which correspond to HOMO or LUMO in similar to those of Figure 2a. Note that $\epsilon_{\rm D}$ of Figure 2a is smaller than that of Figure 2b.

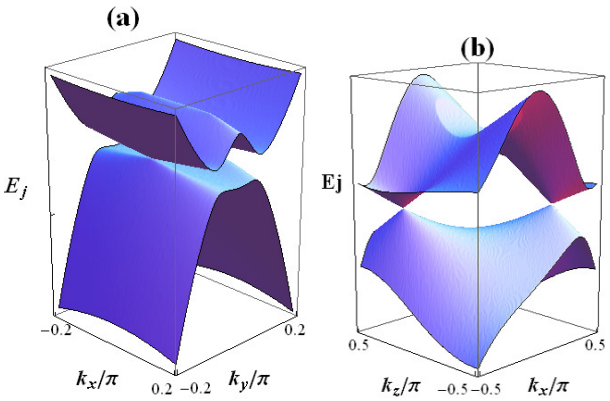

Figure 2. (Color online) (a) Energy band at $k_z = 0$ where the Dirac point is given by $\boldsymbol{k}_{\rm D} = \pm(0, 0.075, 0)\pi$ (b) Energy band at $k_y = 0$ where the Dirac point is given by $\boldsymbol{k}_{\rm D} = \pm(0.344, 0, -0.275)\pi$

 doi:10.20944/preprints202406.0543.v1

3.2. Nodal Line and DOS

Figure 3a shows Dirac points in 3D momentum space forming a nodal line, where A (B) on the line corresponds to a minimum (maximum) of the energy and exists on a plane of $k_z = 0$ ($k_y = 0$). The width of the energy variation along the nodal line is given by ~ 0.002. The chemical potential is located between A and B. The energy is symmetric with respect to the Γ point, $(k_x, k_y, k_z) = (0, 0, 0)$ and $k_x = 0$. Figure 3b shows DOS as function of $\omega - \mu_0$, where μ_0 denotes the chemical potential at T=0. It is found that $D(\mu_0) \neq 0$ due to the nodal line, where the energy varies around μ_0. There is an asymmetry of $D(\omega)$ with respect to $\omega = \mu_0$, which shows $D(\mu_0 - \tilde{\omega}) < D(\mu_0 + \tilde{\omega})$ for $\tilde{\omega} = \omega - \mu_0 > 0.002$, and $D(\mu_0 - \tilde{\omega}) > D(\mu_0 + \tilde{\omega})$ for $\tilde{\omega} < 0.002$ [32] The dashed line denotes $\tilde{D}(\mu_0 + \tilde{\omega})$, which is defined by $D(\mu_0 - \tilde{\omega})$. Noting that $D(\omega) \propto |\omega - \mu_0|$ without tilting of the Dirac cone, which is proportional to the inverse of the averaged velocity of the Dirac cone, [42] the velocity of the valence band ($\tilde{\omega} < 0$) is larger than that of the conduction band ($\tilde{\omega} > 0$) except for the momentum around the the nodal line. The inset denotes the T dependence of $\mu - \mu_0$, which increases slightly for μ close to the nodal line and decreases with increasing T for μ being away from the nodal line.

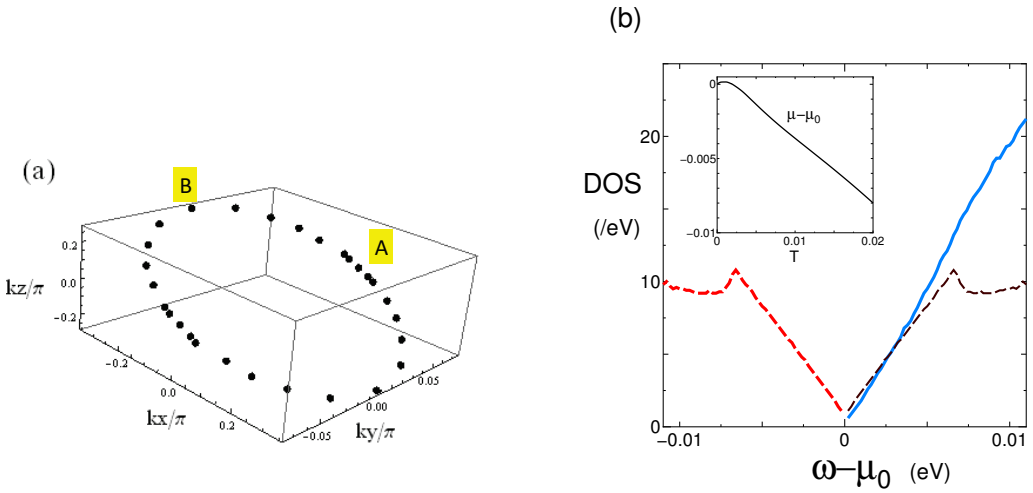

Figure 3. (Color online) Nodal line (a) and DOS (b) [32] (a) Closed circle denotes Dirac point in 3D momentum space (k_x, k_y, k_z), which gives a nodal line. The points A and B on the line correspond to a Dirac point in Figure 2a and Figure 2b respectively. They provide a minimum and a maximum of the energy on the nodal line. The chemical potential exists on the line between A and B. (b)DOS [$D(\omega)$] is shown as a function of $\omega - \mu_0$, where μ_0 denotes the chemical potential at T=0. The dashed line is drawn to compare with the blue line, where the dashed line and the red line is symmetric around $\omega = \mu_0$. Inset denotes the T dependence of $\mu - \mu_0$ with $\mu_0 = 0.5053$.

4. Seebeck Coefficients

Since the present salt of [Pd(dddt)$_2$] shows the largest conductivity along the y–axis, we first examine the Seebeck coefficient S_y. Next we examine S_ν ($\nu = x$ and z) with the direction perpendicular to the y-direction. Further, the mutual relation between the conductivity and the Seebeck coefficient is clarified, where both quantities are determined by the spectral conductivity.

4.1. Coefficient for the y-Axis Direction

Figure 4 shows the conductivity σ_y and the components $\sigma_y^{\gamma\gamma'}$ as a function of T for some choices of Γ_0 = 0.0003 and 0.0005 with $R = 2$. E_5 (E_4) corresponds to the valence band (conduction band), which is given by $\epsilon < \mu_0$ ($\epsilon > \mu_0$). However such a correspondence is invalid in a small region of $|\epsilon - \mu_0| < 0.0002$ due to the variation of the energy on nodal line. It is found that $\sigma_y^{44} > \sigma_y^{55}$ at low temperatures ($T < 0.002$), while $\sigma_y^{44} < \sigma_y^{55}$ at high temperatures ($T > 0.002$). Thus, the contribution from the valence band is larger (smaller) than that from the conduction band at high (low) temperatures. Such a relation can be understood from DOS in Figure 3b, where the average velocity of the Dirac

 doi:10.20944/preprints202406.0543.v1

cone of the conduction band is larger (smaller) than that of the valence band for the electron with $0 < \epsilon - \mu_0 < 0.002$ ($\epsilon - \mu_0 > 0.002$). The component normalized by the total σ_y shows a small dependence on Γ_0 (impurity scattering), while the total one decreases clearly by the increase of Γ_0.

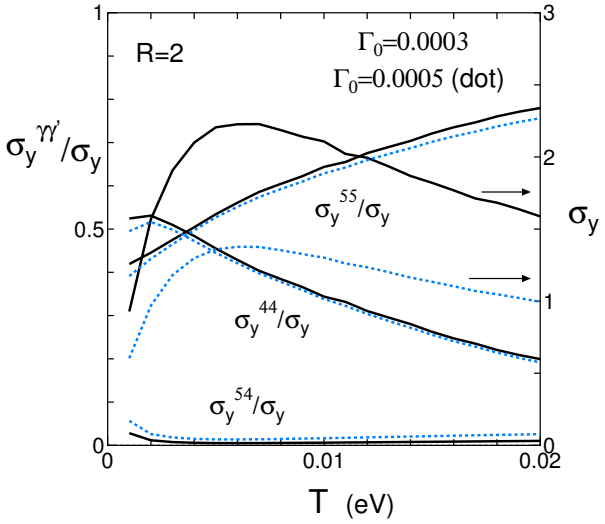

Figure 4. (Color online) T dependence of the conductivity σ_y (right axis) and the components $\sigma_y^{\gamma\gamma'}$ (left axis) for Γ_0 = 0.0003 (solid line) and 0.0005 (dotted line) with $R = 2$, where $\sigma_y = \sigma_y^{44} + \sigma_y^{55} + \sigma_y^{54} + \sigma_y^{45}$. Quantities σ_y^{44}/σ_y and σ_y^{55}/σ_y (σ_y^{45}/σ_y and σ_y^{54}/σ_y) correspond to intraband (interband) contribution.

In Figure 5, the Seebeck coefficient S_y ($\Gamma_0 = 0.0003$ and 0.0005) is examined with some choices of $R = 1$, 2 and 4. It turns out that there is a sign change of S_y around $T \simeq 0.006$, where $S_y(> 0)$ at high temperatures takes a maximum and $S_y(< 0)$ at low temperatures takes a minimum. At high temperatures, S_y decreases with the increase of R due to the effect of the e–p interaction, which is enhanced by the increase of T as seen from Equation (15a). Note that S_y for $T \simeq 0.008$ is almost independent of R. At low temperatures, S_y reduces to zero in the limit of $T \to 0$ as seen from Equations (21) and (22) [39]. The Seebeck coefficient S_y with $\Gamma_0 = 0.0003$ is compared with $\Gamma_0 = 0.0005$. The increase of Γ_0 reduces $S_y(> 0)$ implying that the reduction of L_{12}^y is larger than that of L_{11}^y. The temperature corresponding to the sign change ($S_y = 0$) decreases for increasing R, but remains almost the same for the increase of Γ_0.

Figure 6 shows the components of the Seebeck coefficients $S_y^{\gamma\gamma'}$ and S_y for $\Gamma_0 = 0.0003$ with $R = 2$. $S_y^{44}(< 0)$ comes from the conduction band with $\epsilon > \mu_0$, which is obtained from LUMO band outside the nodal line and from HOMO band inside the nodal line. $S_y^{55}(> 0)$ comes from the valence band with $\epsilon < \mu_0$, which is given by HOMO band outside the nodal line and by LUMO band inside the nodal line The off diagonal component $S_y^{45}(= S_y^{54})$ is negligibly small compared with the diagonal components S_y^{44} and S_y^{55}. The total contribution $S_y(= S_y^{44} + S_y^{55})$ is shown by the right hand axis, where $S_y < 0$ at low temperatures and $S_y > 0$ at high temperatures and $S_y = 0$, i.e., the sign change occurs at $T \sim 0.006$. The dotted line denotes $-S_y^{44}$ and is compared with S_y^{55}, where their intersection gives $Sy = 0$.

 doi:10.20944/preprints202406.0543.v1

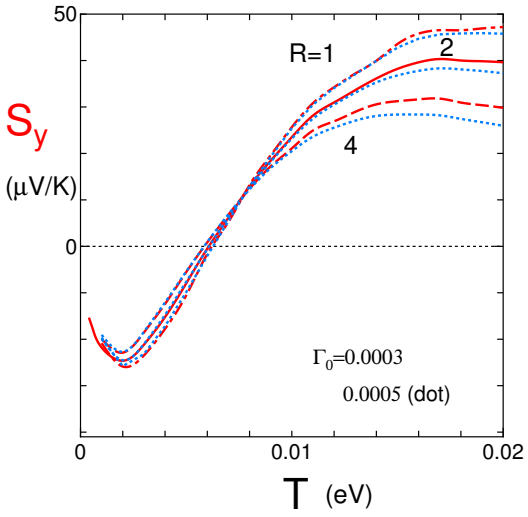

Figure 5. (Color online) T dependence of the Seebeck coefficient S_y with $R = 1$ (dot-dashed line), 2(solid line) and 4(dashed line) for $\Gamma_0 = 0.0003$ and 0.0005(dot).

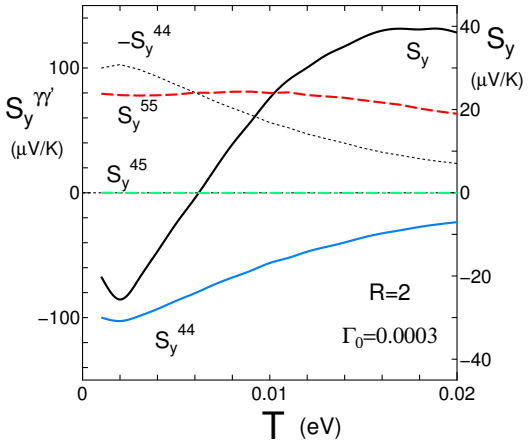

Figure 6. (Color online) T dependence of the components of the Seebeck coefficients $S_y^{\gamma\gamma'}$ and S_y for $\Gamma_0 = 0.0003$ with $R = 2$. S_y^{44} is negative due to the conduction band with $\epsilon > \mu_0$, while S_y^{55} is positive due to the valence band with $\epsilon < \mu_0$. The interband component S_y^{45} is negligibly small compared with the intraband components S_y^{44} and S_y^{55}. The total contribution $S_y (= S_y^{44} + S_y^{55})$ is shown by the right hand axis, where $S_y < 0$ at low temperatures and $S_y > 0$ at high temperatures leading to $S_y = 0$ at $T \sim 0.006$. The $-S_y^{44}$ (dotted line) is shown to compare with S_y^{55}.

4.2. Coefficients for the x and z-Axes Directions

Figure 7 shows $S_\nu(T)$ and $\sigma_\nu(T)$ for $\nu = x$ and z. The conductivity σ_ν with $\nu = x$ and z is much smaller than σ_y due to the large anisotropy of the velocity $v_x, v_z << v_y$, since the transfer energy for the y axis is largest due to the molecular stacking direction. Both $S_x(> 0)$ and $S_z(> 0)$ show no sign change. The fact that $\sigma_z(T) > \sigma_x(T)$ and $S_x > S_z$ at high temperatures suggests that the effect of the conductivity is larger than that of the thermal conductivity. At high temperatures, $S_x(T)$ is much larger than S_z and S_z decreases rapidly. Note that S_x takes a minimum at low T and $S_x \simeq 0$ at $T \simeq 0.002$. Such a minimum suggests that S_x is close to the sign change as discussed later.

Figure 8 shows components of the normalized conductivity $\sigma_\nu^{\gamma\gamma'}/\sigma_\nu$ with $\nu = x$ (solid line) and z (dashed line) for $\Gamma_0 = 0.0003$ and $R = 2$. The total conductivity is given by σ_ν ($= \sigma_\nu^{44} + \sigma_\nu^{55} + \sigma_\nu^{54} + \sigma_\nu^{45}$). Quantities $\sigma_\nu^{44}/\sigma_\nu$ and $\sigma_\nu^{55}/\sigma_\nu$ ($\sigma_\nu^{45}/\sigma_\nu$ and $\sigma_\nu^{54}/\sigma_\nu$) correspond to intraband (interband) contribution, where the interband contribution is negligibly small. The difference between σ_ν^{55} (the valence band) and σ_ν^{44} (conduction band) increases by the increase of T. The difference between $\sigma_x^{\gamma\gamma'}/\sigma_x$ and $\sigma_z^{\gamma\gamma'}/\sigma_z$

 doi:10.20944/preprints202406.0543.v1

is small compared with that between σ_x and σ_z. Thus, the main contribution for the conductivity is given by the valence band at high temperatures.

Figure 9 shows components of Seebeck coefficient $S_\nu^{\gamma\gamma'}(T)$ for $\nu = x$ and z, which are mainly determined by the intraband contributions, i.e., S_ν^{55} and S_ν^{44}. The contribution from the valence band S_ν^{55} has a positive sign and that of the conduction band S_ν^{44} has a negative sign. The total Seebeck coefficient has a positive sign due to $S_\nu^{55} > |S_\nu^{44}|$. The difference between S_x^{44} and S_z^{44} is negligibly small, while S_x^{55} is larger than S_z^{55} except for low temperatures. The minimum of S_x at $T \simeq 0.002$ in Figure 7 is compatible with a fact that $S_x^{55} \simeq -S_x^{44}$ at low temperatures in Figure 9 (the solid line is compared with the dotted line).

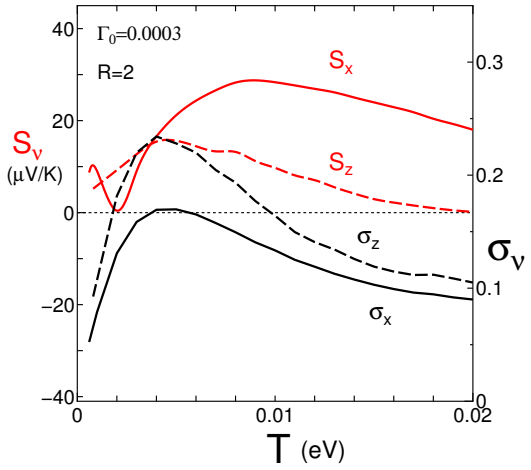

Figure 7. (Color online) Seebeck coefficient $S_\nu(T)$ and conductivity $\sigma_\nu(T)$ for $\nu = x$ and z with fixed $\Gamma_0 = 0.0003$ and $R = 2$.

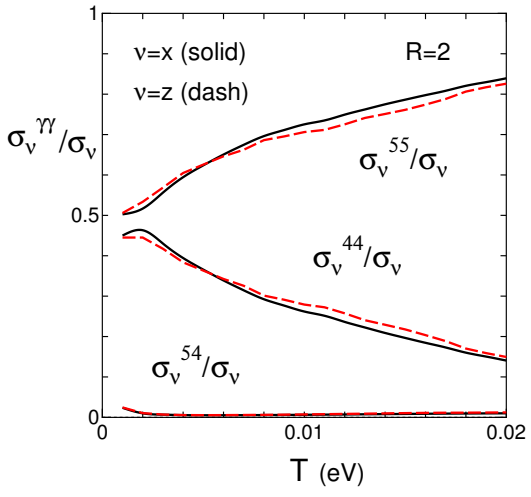

Figure 8. (Color online) Components of the normalized conductivity $\sigma_\nu^{\gamma\gamma'}/\sigma_\nu$ with $\nu = x$ (solid line) and z (dashed line) for $\Gamma_0 = 0.0003$ and $R = 2$, where $\sigma_\nu = \sigma_\nu^{44} + \sigma_\nu^{55} + \sigma_\nu^{54} + \sigma_\nu^{45}$. Quantities $\sigma_\nu^{44}/\sigma_\nu$ and $\sigma_\nu^{55}/\sigma_\nu$ ($\sigma_\nu^{45}/\sigma_\nu$ and $\sigma_\nu^{54}/\sigma_\nu$) correspond to intraband (interband) contribution.

 doi:10.20944/preprints202406.0543.v1

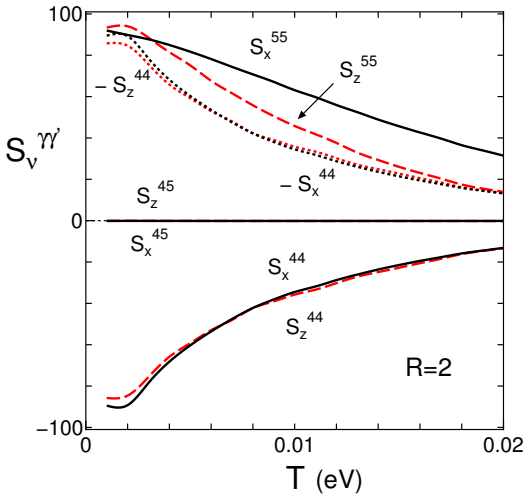

Figure 9. (Color online) Components of Seebeck coefficient $S_\nu^{\gamma\gamma'}(T)$ for $\nu = x$ and z as a function of T.

4.3. Spectral Conductivity

The Seebeck coefficient is obtained from the spectral conductivity, which is expanded in terms of $\epsilon - \mu$. From Equations (21) and (22), the Seebeck coefficient is written as

$$S_\nu(T) = -\frac{\pi^2 T}{3e} \times \frac{\sigma_\nu'(\mu,T) + (7\pi^2/30)\sigma_\nu'''(\mu,T)T^2 + \cdots}{\sigma_\nu(\mu,T) + (\pi^2/6)\sigma_\nu''(\mu,T)T^2 + \cdots}. \tag{23}$$

In the limit of low T, the sign of $S_y(T)$ is determined by that of $-\sigma_y{}'(\mu,T)$ due to $S_y(T) \simeq -(\pi^2/3e)T\sigma_y{}'(\mu,T)/\sigma_y(\mu,T)$. Since the sign change of S_ν is determined by zero of the numerator, the temperature for the sign change deviates slightly from that of $\sigma'(\mu,T) = 0$. In Figure 10a,b, spectral conductivities $\sigma_\nu(\epsilon,T)$ are shown as a function of $\epsilon - \mu_0$.

Figure 10a presents $\sigma_y(\epsilon,T)$, which takes a minimum at $\epsilon = \epsilon_{\rm min}$. The variation of $\sigma_y(\epsilon,T)$ at low temperatures is small for $|\epsilon - \mu_0| < 0.0002$, which corresponds to the energy region of the nodal line. A linear increase of $\sigma_y(\epsilon,T)$ for $|\epsilon - \mu_0| > 0.0002$, can be understood from the increase of DOS [Figure 3b]. When T increases, $\epsilon_{\rm min}(< 0)$ increases to zero and $\sigma_y(\epsilon,T)$ at $\epsilon = \epsilon_{\rm min}$ increases slowly. However for ϵ being away from $\epsilon_{\rm min}$, the opposite behavior of the T dependence of $\sigma_y(\epsilon,T)$ is found, i.e., $\sigma_y(\epsilon,T)$ decreases with increasing T. These two behaviors can be understood from Equation (12). The T dependence of $\sigma_y(\epsilon,T)$ is determined by that of Γ_γ, which increases by T as shown in Equations (14) and (15a). From Equation (12), the numerator gives the increase of $\sigma_y(\epsilon,T)$ at $\epsilon = \epsilon_{\rm min}$, while the denominator gives the decrease of $\sigma_y(\epsilon,T)$ at ϵ being far away from $\epsilon_{\rm min}$. Such a mechanism also explains the T dependence of the conductivity σ_y in Figure 4, which increases at low T but decreases at high T. The vertical lines denote the corresponding $\mu(T)$, where $\mu(0)$ is shown by the solid line. $\mu(T)$ increases for $0 < T < 0.001$ and decreases for $0.001 < T$ as shown in the inset of Figure 3(b). Since $\sigma_y{}'(\mu,T) > 0$ for $0 < T < 0.002$ and $\sigma_y{}'(\mu,T) < 0$ at $T = 0.004$, T corresponding to $\sigma_y{}'(\mu,T) = 0$ is lower than that of the sign change of $S_y = 0$ (Figure 5), i.e., $T \simeq 0.006$. Such a discrepancy suggests that the second term of Equation (22) becomes relevant with increasing T. Figure 10b presents the $\epsilon - \mu_0$ dependence of $\sigma_\nu(\epsilon,T)$ for $\nu = x$ and z, which takes a minimum at $\epsilon = \epsilon_{\rm min}$. Since $\epsilon_{\rm min} > \mu(T)$ is found at any T, $\sigma_\nu{}'(\mu,T) < 0$ at finite temperatures suggests $S_\nu(T) > 0$, i.e., no sign change of the Seebeck coefficient. At $T \simeq 0.002$, the unequality of $|\sigma_x{}'(\mu,T)| < |\sigma_z{}'(\mu,T)|$ suggests $S_x(T) < S_z(T)$, while the effect of the higher order of Equation (22) may give rise to a minimum of $S_x(T)$ in Figure 7.

 doi:10.20944/preprints202406.0543.v1

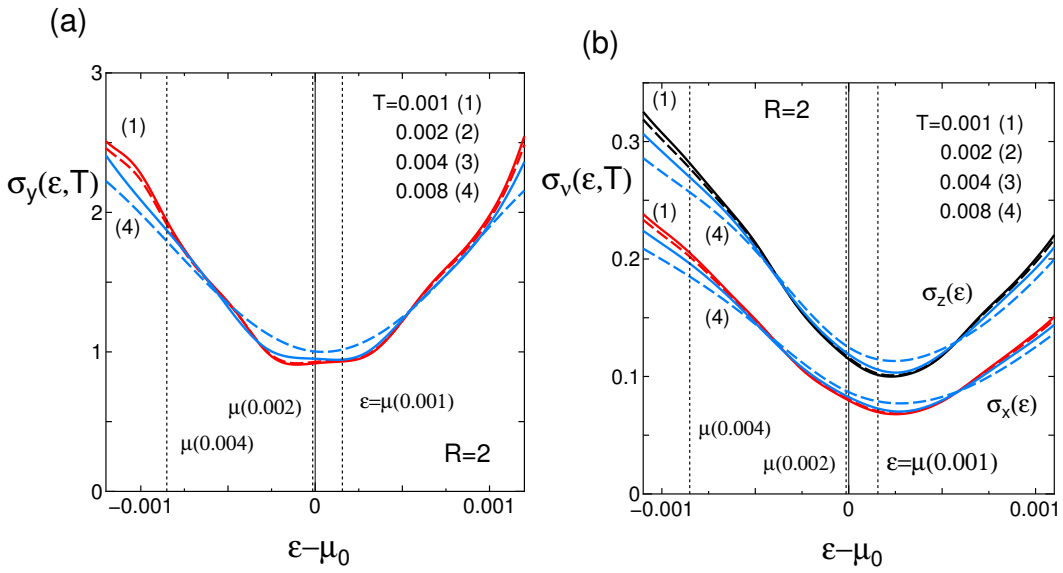

Figure 10. (Color online) Spectral conductivity $\sigma_y(\epsilon, T)$ as a function of $\epsilon - \mu_0$ with $\Gamma_0 = 0.0003$ and $R = 2$ for T = 0.001(1), 0.002 (2), 0.004, and 0.008 (4). The vertical lines denote $\mu - \mu_0$ for the corresponding T. T = 0 and 0.002.

5. Summary and Discussion

In summary, we calculated the T dependence on the Seebeck coefficient $S_\nu(T)$ ($\nu = y, x$ and z) of the molecular conductor [Pd(dddt)$_2$] under a high pressure and examined in terms of the spectral conductivity $\sigma_\nu(\mu, T)$. The conductor exhibits the largest conductivity along the y direction corresponding to the molecular stacking, where the z axis is perpendicular to a two-dimensional y–z plane.

Noticeable behavior is found in the T dependence of $S_y(T)$. With decreasing T, $S_y(T)$ changes the sign from the positive to negative one as seen from Figure 5. This implies the crossover of the dominant contribution from the hole of the valence band (E_5) to the electron of the conduction band (E_4) (Figure 6). The Seebeck coefficient S_y in Figure 5 is determined by the $\boldsymbol{k}$ dependence of the velocity $v^y_{\gamma\gamma'}$. The sign change is also understood from the energy dependence of DOS being proportional to the inverse of the averaged velocity [Figure 3b], where the average velocity of the conduction (valence) band is larger than that of the valence (conduction) band close to (away from) $\omega = \mu_0$. This is quantitatively understood from the crossover of the component of the conductivity (Figure 4), where $\sigma_y^{44} > \sigma_y^{55}$ at lower temperatures and $\sigma_y^{55} > \sigma_y^{44}$ at higher temperatures. The result of $S_y(T) < 0$ at low temperature is consistent with the spectral conductivity at low temperature (Figure 10a), i.e., $\sigma_y{}'(\mu, T) > 0$ at T = 0.001. Note that such a sign change has been also found for α-(BEDT-TTF)$_2$I$_3$ under a uniaxial pressure, [39] which is understood from the components of the conductivity and the spectral conductivity. However, the relevance of the Seebeck coefficient to the asymmetry of the Dirac cone is unclear in the case of the uniaxial pressure.

Finally, we note the T dependence of S_ν with $\nu = x$ and z. There is a large anisotropy of the conductivity, where σ_x and σ_z are much smaller than σ_y suggesting that the velocity for x and z are much smaller than that for y. In this case, it is complicated to discuss the Seebeck coefficient in terms of the ω dependence of DOS. In fact, there is no change of the sign at low temperatures, i.e., $S_x > 0$ and $S_z > 0$ (Figure 7) implying that the contribution from the valence band is always larger than that from the conduction band (Figures 8 and 9). No sign change at low temperature is also understood from the spectral function, where $\sigma_y{}'(\mu, T) < 0$ at low temperatures (Figure 10b). This result shares a common feature with the Seebeck coefficient of the α-(BEDT-TTF)$_2$I$_3$ under a hydrostatic pressure, where the hole-like behavior at finite temperatures with the zero doping is obtained [40].

 doi:10.20944/preprints202406.0543.v1

Acknowledgments: The author thanks M. Ogata for useful discussions on the present work.

References

1. K. S. Novoselov, A. K. Geim, S. V. Morozov, D. Jiang, M. I. Katsnelson, I. V. Grigorieva, S. V. Dubonos, and A. A. Firsov, Nature **438**, 197 (2005).
2. K. Kajita, Y. Nishio, N. Tajima, Y. Suzumura, and A. Kobayashi, J. Phys. Soc. Jpn. **83**, 072002 (2014).
3. R. Kato, H. B. Cui, T. Tsumuraya, T. Miyazaki, and Y. Suzumura, J. Am. Chem. Soc. **139**, 1770 (2017).
4. S. Katayama, A. Kobayashi, and Y. Suzumura, J. Phys. Soc. Jpn. **75**, 054705 (2006).
5. A. Kobayashi, S. Katayama, K. Noguchi, and Y. Suzumura, J. Phys. Soc. Jpn. **73**, 3135 (2004).
6. T. Mori, A. Kobayashi, Y. Sasaki, H. Kobayashi, G. Saito, and H. Inokuchi, Chem. Lett. **13**, 957 (1984).
7. R. Kondo, S. Kagoshima, and J. Harada, Rev. Sci. Instrum. **76**, 093902 (2005).
8. R. Kondo, S. Kagoshima, N. Tajima, and R. Kato, J. Phys. Soc. Jpn. **78**, 114714 (2009).
9. H. Kino and T. Miyazaki, J. Phys. Soc. Jpn. **75**, 034704 (2006).
10. A. Kobayashi, S. Katayama, Y. Suzumura, and H. Fukuyama, J. Phys. Soc. Jpn. **76**, 034711 (2007).
11. M. O. Goerbig, J.-N. Fuchs, G. Montambaux, and F. Piéchon,Phys. Rev. B **78**, 045415 (2008).
12. A. Kobayashi, Y. Suzumura, and H. Fukuyama, J. Phys. Soc. Jpn. **77**, 064718 (2008).
13. N. Tajima, R.. Kato, S. Sugawara, Y. Nishio, and K. Kajita, Phys. Rev. B **85**, 033401 (2012).
14. N. H. Shon and T. Ando, J. Phys. Soc. Jpn. **67**, 2421 (1998).
15. N. M. R. Peres, F. Guinea, and A. H. Castro Neto, Phys. Rev. B **83**,125411 (2006).
16. K. Kajita, T. Ojiro, H. Fujii, Y. Nishio, H. Kobayashi, A. Kobayashi, and R. Kato, J. Phys. Soc. Jpn. **61**, 23 (1992).
17. N. Tajima, M. Tamura, Y. Nishio, K. Kajita, and Y. Iye, J. Phys. Soc. Jpn. **69**, 543 (2000).
18. N. Tajima, A. Ebina-Tajima, M. Tamura, Y. Nishio, and K. Kajita, J. Phys. Soc. Jpn. **71**, 1832 (2002).
19. N. Tajima, S. Sugawara, M. Tamura, R. Kato, Y. Nishio, and K. Kajita, EPL **80**, 47002 (2007).
20. D. Liu, K. Ishikawa, R. Takehara, K. Miyagawa, M. Tanuma, and K. Kanoda, Phys. Rev. Lett. **116**, 226401 (2016).
21. Y. Suzumura and M. Ogata, Phys. Rev. B **98**, 161205 (2018).
22. H. B. Cui, T. Tsumuraya, Y. Kawasugi, R. Kato R. presented at 17th Int. Conf. High Pressure in Semiconductor Physics (HPSP-17), (2016).
23. T. Tsumuraya, H. B. Cui, T. Miyazaki, R. Kato, presented at Meet. Physical Society Japan, (2014).
24. R. Kato and Y. Suzumura, J. Phys. Soc. Jpn. **86**, 064705 (2017).
25. S. Murakami, New J. Phys. **9** 356 (2007).
26. M. Hirayama, R. Okugawa, S. Murakami, J. Phys. Soc. Jpn. **87**, 041002 (2018).
27. A. Bernevig, H. Weng, Z. Fang, X. Dai, J. Phys. Soc. Jpn. **2018**, **87**, 041001 (2018).
28. Z. Liu, H. Wang, Z.F. Wang, J. Yang, F. Liu, Phys. Rev. B **97**, 155138 (2018).
29. T. Tsumuraya, R. Kato, Y. Suzumura, J. Phys. Soc. Jpn. **87**, 113701 (2018).
30. Y. Suzumura, H. B. Cui, R. Kato, J. Phys. Soc. Jpn. **87**, 084702 (2018).
31. R. Kato, H. Cui, T. Minamidate, H. H.-M. Yeung, and Y. Suzumura, J. Phys. Soc. Jpn. **89**,124706 (2020)
32. Y. Suzumura, R. Kato, and M. Ogata, Crystals **10**, 862 (2020). see also http://arxiv.org/abs/2009.05272.
33. R. Kubo, J. Phys. Soc. Jpn. **12**, 570 (1957).
34. J. M. Luttinger, Phys. Rev. **135**, A1505 (1964).
35. M. Ogata and H. Fukuyama, J. Phys. Soc. Jpn. **88**, 074703 (2019).
36. R. Kitamura, N. Tajima, K. Kajita, R. Reizo, M. Tamura, T. Naito, and Y. Nishio, JPS Conf. Proc..**1**, 012097 (2014); N. Tajima, private communication.
37. T. Konoike, M. Sato, K. Uchida, and T. Osada, J. Phys. Soc. Jpn. **82**, 073601 (2013).
38. D. Ohki, Y. Omori, and A. Kobayashi. Phys. Rev. B **101**, 245201 (2020)
39. Y. Suzumura and M. Ogata, Phys. Rev. B **107**, 195416 (2023).
40. Y. Suzumura, T. Tsumuraya and M. Ogata, J. Phys. Soc. Jpn. **93**, 054704 (2024).
41. H. Fröhlich, Proc. Phys. Soc. A **223**, 296 (1954).
42. S. Katayama, A. Kobayashi, and Y. Suzumura, J. Phys. Soc. Jpn. **75**, 023708 (2006).
43. A. A. Abrikosov, L. P. Gorkov, and I. E. Dzyaloshinskii, *Methods of Quantum Field Theory in Statistical Physics* (Prentice-Hall, Englewood Cliffs, NJ, 1963).

 doi:10.20944/preprints202406.0543.v1

44. M.J. Rice, L. Pietronero, and P. Brüesh, Solid State Commun. **21**, 757 (1977).
45. H. Gutfreund, C. Hartzstein, and M. Weger Solid State Commun. **36**, 647 (1980).